Letters

An Adaptive-Frequency Harmonic Suppression Strategy Based on Vector Reconstruction for Current Measurement Error of PMSM Drives

Yin Bai, Binxing Li, Qiwei Wang, Dawei Ding, Guoqiang Zhang, *Senior Member, IEEE*, Gaolin Wang, *Senior Member, IEEE*, and Dianguo Xu, *Fellow, IEEE*

***Abstract*—The errors of gain and offset caused by the current sensor measurement can lead to the first and second harmonics in *dq*-axis currents of the permanent magnet synchronous motor (PMSM) drives. An adaptive-frequency harmonic suppression strategy based on the vector reconstruction for current measurement error is proposed. The *dq*-axis current vector is recoordinate transformed using the division-frequency position as the transformation matrix angle. Thus, the frequency of the fundamental component can be decoupled from that of the harmonics in the current vector. In this way, the single-frequency harmonic suppressor can be established in the reconstructed coordinate frame. The current vector error is converged by adaptively adjusting the filtering weight and frequency so as to eliminate the harmonics. In view of the change of fundamental frequency, the variable step of the convergence is used to obtain the ideal filtering effect at different speeds and reduce the negative impact of current sensor measurement errors. The effectiveness of the proposed method is verified on the 11.7-kW PMSM drive platform.**

***Index Terms*—Current measurement error (CME), current sensor, permanent magnet synchronous motor (PMSM), single-frequency harmonic suppression.**

I. Introduction

PERMANENT magnet synchronous motor (PMSM) is widely used in industrial production due to its high efficiency, high power factor, and good dynamic performance [1]. In the PMSM drive system, the current harmonics caused by the current measurement errors (CMEs) of the phase current sensors result in the vibration and torque fluctuations of the motor affecting the operating condition of PMSM [2]. Thus, it is crucial to suppress the current harmonics caused by the CMEs.

Manuscript received 29 May 2022; revised 11 July 2022 and 10 August 2022; accepted 18 August 2022. Date of publication 22 August 2022; date of current version 10 October 2022. This work was supported in part by the Research Fund for the National Natural Science Foundation of China under Grant 52125701 and Grant 52177034, and in part by the Fundamental Research Funds for the Central Universities FRFCU5710092020. *(Corresponding author: Binxing Li.)*

The authors are with the School of Electrical Engineering and Automation, Harbin Institute of Technology, Harbin 150001, China (e-mail: baiyinhit@163.com; li_binxing@163.com; wqw0543@163.com; dingdawei@hit.edu.cn; ZHGQ@hit.edu.cn; WGL818@hit.edu.cn; xudiang@hit.edu.cn).

Color versions of one or more figures in this article are available at https://doi.org/10.1109/TPEL.2022.3200708.

Digital Object Identifier 10.1109/TPEL.2022.3200708

The research for suppressing the current harmonics due to the CMEs can be divided into two main categories: the periodic harmonic suppression and the adaptive filtering methods. The periodic harmonic suppression method extracts the harmonics in one fluctuation cycle, and injects it into the current feedback to achieve the harmonic elimination. Since the *dq*-axis current harmonics are integer multiples of the electric frequency, the total harmonics show periodic variations. Hence, the current harmonics can be suppressed by the periodic harmonic suppression methods, such as the iterative learning control [3], the repetitive control [4], and the proportional resonance control [5]. The periodic harmonic suppression method does not need to identify the harmonic components and can suppress the total harmonic content as the overall periodic disturbance [6]. However, the harmonic suppression effect diminishes for the high-frequency disturbance, and the design method is complicated and is not strong to the robustness.

The adaptive filtering method mainly includes the notch filter [7], SOGI filter [8], and ADALINE filter [9]. The adaptive filter is used to eliminate the specific-frequency harmonics in the current, which is better stability robustness [10]. An adaptive notch filter is presented in [7] to diminish the current harmonics. In [8], a kind of cascaded SOGI filter is used to improve the control accuracy of the PMSM. In [9], the current feedback could be filtered by a second-order ADALINE filter to suppress the period disturbance.

The adaptive filter is widely used in the sensorless motor drive, which is commonly adopted to suppress the harmonics in the back electromotive force (EMF) [11], [12], [13], [14]. The RLS filter was presented in [11] to eliminate the fifth and seventh harmonics caused by the nonlinear effect of the inverter. In [12], an adaptive observer was used to reduce the negative influence of the dc offset in the back EMF. On this base, the adaptive comb filter is proposed to filter the ac harmonics of the back EMF in [13]. In [14], the adaptive notch filter was used, which overcomes the dependence of frequency convergence on the signal amplitude and the problem of double-frequency oscillation in the estimated frequency. The adaptive filter requires the information of the harmonic frequencies since each harmonic is extracted and eliminated separately. If there exist more frequencies of harmonics, the structure of the filtering network will be complex.

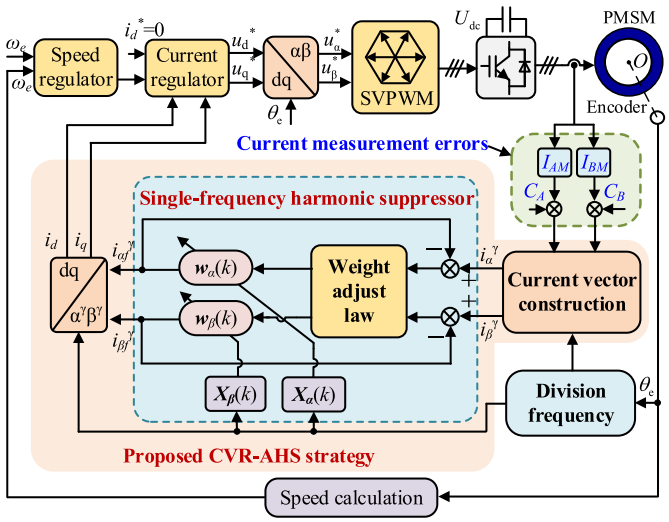

Fig. 1. Block diagram of PMSM drive using proposed method.

In this letter, an adaptive-frequency harmonic suppression strategy based on the current vector reconstruction (CVR-AHS) for PMSM drives is proposed to restrain the negative influence due to the CME. First, the *dq*-axis current vector is recoordinate transformed with the division-frequency position as the transformation-matrix angle to decouple the frequencies of the fundamental component and the harmonic components. Then, the single-frequency current harmonic suppressor is constructed in the framework of the reconstructed coordinate system. The error of the reconstructed current vector is converged by adjusting the fundamental frequency adaptively and filtering the weights to filter the harmonics. Meanwhile, the variable convergence step is used to ensure the filtering effect at different speeds to realize the adaptive frequency adjustment of the algorithm. Experiments are conducted in the 11.7-kW PMSM drive system to verify the effectiveness of the proposed method.

II. Proposed Current Harmonic Suppression Strategy Based on Current Vector Reconstruction

The block diagram of the PMSM control system using the proposed CVR-AHS strategy based on the current vector reconstruction is shown in Fig. 1, where I_{AM} and I_{BM} are the gain of the measurement of *A*- and *B*-phase currents, respectively, and C_A and C_B are the offset of the measurement of *A*- and *B*-phase currents, respectively. The strategy mainly consists of the current vector reconstruction and the single-frequency harmonic suppressor. The whole strategy takes the reconstructed coordinate system as the framework. The single-frequency harmonic suppressor is designed in the new coordinate frame to filter the reconstructed current vector, which is then mapped in the *dq*-axis coordinate frame as the current feedback through the coordinate transformation.

A. Current Vector Reconstruction Strategy

The errors of the gain and offset by the CMEs lead to the first and second harmonics of *dq*-axis currents in the PMSM control system [2]. The *dq*-axis currents considering the CMEs can be expressed as

$$\boldsymbol{i}_{\boldsymbol{sM}}^{\boldsymbol{dq}} = \boldsymbol{i}_{\boldsymbol{s}}^{\boldsymbol{dq}} + I_1\boldsymbol{I}_{\boldsymbol{s1}} + I_2\boldsymbol{I}_{\boldsymbol{s2}} + \boldsymbol{I}_{\boldsymbol{dc}} \tag{1}$$

where $\boldsymbol{i}_{\boldsymbol{sM}}^{\boldsymbol{dq}} = [i_{dM}\, i_{qM}]^T$ is the *dq*-axis current vector considering the CMEs, $\boldsymbol{i}_{\boldsymbol{s}}^{\boldsymbol{dq}} = [i_{\mathrm{d}}\ i_{\mathrm{q}}]^T$ is the dc vector of the *dq*-axis currents, $\boldsymbol{I}_{\boldsymbol{s1}} = [\sin(-\theta_{\mathrm{e}}+\varphi_1)\ \cos(-\theta_{\mathrm{e}}+\varphi_1)]^T$ is the first current harmonic vector, $\boldsymbol{I}_{\boldsymbol{s2}} = [\sin(-2\theta_{\mathrm{e}}+\varphi_2)\ \cos(-2\theta_{\mathrm{e}}+\varphi_2)]^T$ is the second current harmonic vector, $\boldsymbol{I}_{\boldsymbol{dc}} = [I_{\mathrm{d}}\ I_{\mathrm{q}}]^T$ is the offset of *dq*-axis currents due to the CMEs, and I_1, φ_1, I_2, φ_2 are the amplitudes and the phases of the first and second current harmonics, respectively. In the control system, the model of *dq*-axis current is a closed-loop negative feedback control system, where the current harmonics generated by the CMEs are coupled in the current feedback. When the motor runs in the steady state, the current feedback can follow the current reference until the same. Thus, the dc component $\boldsymbol{I}_{\boldsymbol{dq}}$ in the current feedback can be suppressed by tracking the current reference. However, the first and second harmonics are ac components, which cannot be suppressed by the current loop. Although the current loop has the filtering effect, the high bandwidth of the current loop is difficult to filter out the effect at low-frequency harmonics. Therefore, the first and second harmonics still need to be further processed.

Through the coordinate transformation, the $\alpha\beta$-axis currents can be expressed by the *dq*-axis currents as

$$\boldsymbol{i}_{\boldsymbol{s}}^{\boldsymbol{\alpha\beta}} = \boldsymbol{T}_{\boldsymbol{rs}}(\theta_e)\cdot\boldsymbol{i}_{\boldsymbol{s}}^{\boldsymbol{dq}} = \sqrt{i_d^2+i_q^2}\,\boldsymbol{I}_{\boldsymbol{s}} \tag{2}$$

where $\boldsymbol{i}_{\boldsymbol{s}}^{\boldsymbol{\alpha\beta}} = [i_\alpha\ i_\beta]^T$ is the $\alpha\beta$-axis current vector, $\boldsymbol{I}_{\boldsymbol{s}} = [\sin(\theta_e+\varphi_s)\ \cos(\theta_e+\varphi_s)]^T$ is the unit current vector, $\varphi_s = \tan^{-1}(i_q/i_d)$ is the phase of $\boldsymbol{I}_{\boldsymbol{s}}$, and $\boldsymbol{T}_{\boldsymbol{rs}}(\theta_e)$ is the transformation matrix with θ_e as the angle, which is shown as

$$\boldsymbol{T}_{\boldsymbol{rs}}(\theta_e) = \begin{bmatrix} \cos\theta_e & -\sin\theta_e \\ \sin\theta_e & \cos\theta_e \end{bmatrix}. \tag{3}$$

The $\alpha\beta$-axis currents considering the CMEs can be expressed as

$$\begin{aligned}\boldsymbol{i}_{\boldsymbol{sM}}^{\boldsymbol{\alpha\beta}} &= \boldsymbol{T}_{\boldsymbol{rs}}(\theta_e)\cdot\boldsymbol{i}_{\boldsymbol{sM}}^{\boldsymbol{dq}} \\ &= \sqrt{(i_d+i_q)^2 + I_2^2(1-2\sin 2\varphi_2)}\,\boldsymbol{I}_{\boldsymbol{s}} + I_1\boldsymbol{I}_{\boldsymbol{\varphi}}\end{aligned} \tag{4}$$

where $\boldsymbol{i}_{\boldsymbol{sM}}^{\boldsymbol{\alpha\beta}} = [i_{\alpha M}\, i_{\beta M}]^T$ is $\alpha\beta$-axis current vector considering the CMEs, $\boldsymbol{I}_{\boldsymbol{\varphi}} = [\sin\varphi_M\ \cos\varphi_M]^T$ is the dc component, and $\varphi_M = \tan^{-1}(i_{qM}/i_{dM})$ is the phase of $\boldsymbol{I}_{\boldsymbol{\varphi}}$. According to (4), the first harmonics of *dq*-axis currents result in the offset error of $\alpha\beta$-axis currents, and the second harmonics result in the change of $\alpha\beta$-axis currents' amplitude. The harmonics decoupled in the amplitude and the offsets of $\alpha\beta$-axis currents are difficult to be filtered, thus the harmonic currents need to be reprocessed.

It is worth noting that a new kind of coordinate frame can be defined to make the rotation frequency of the current vector different from that of the first and second harmonics in the new coordinate frame. In this case, the decoupling of the fundamental and harmonic frequencies in the new coordinate frame can be achieved. Define the rotation frequency of the *dq*-axis current vector as ω_e/n in the new coordinate frame, where $\omega_e = d\theta_e/dt$,

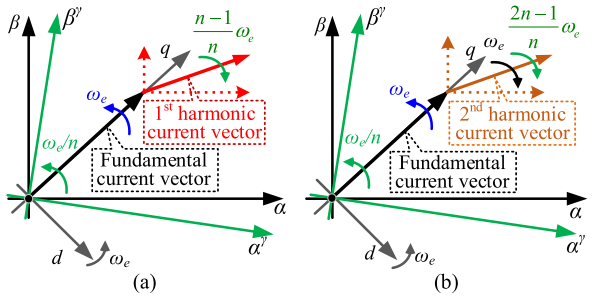

Fig. 2. Relationship of current vectors in *dq*-axis, $\alpha\beta$-axis, and $\alpha^{\gamma}\beta^{\gamma}$-axis frame. (a) First harmonic. (b) Second harmonic.

and n is a positive constant. The $\alpha\beta$-axis frame is converted into the reconstructed axis with θ_e/n as the angle, which is defined as $\alpha^{\gamma}\beta^{\gamma}$-axis. The $\alpha\beta$-axis currents in the $\alpha^{\gamma}\beta^{\gamma}$-axis frame can be shown as

$$\boldsymbol{i}_{\boldsymbol{s}}^{\boldsymbol{\gamma}} = \boldsymbol{T}_{\boldsymbol{rs}}((n-1)\theta_e/n)\cdot \boldsymbol{i}_{\boldsymbol{sM}}^{\boldsymbol{\alpha\beta}} \tag{5}$$

where $\boldsymbol{i}_{\boldsymbol{s}}{}^{\gamma} = [i_{\alpha}{}^{\gamma}\ i_{\beta}{}^{\gamma}]^T$ is the current vector in $\alpha^{\gamma}\beta^{\gamma}$-axis frame. The *dq*-axis currents in $\alpha^{\gamma}\beta^{\gamma}$-axis frame can be expressed as

$$\boldsymbol{i}_{\boldsymbol{s}}^{\boldsymbol{\gamma}} = \underbrace{\boldsymbol{T}_{\boldsymbol{rs}}(\theta_e/n)\cdot \boldsymbol{i}_{\boldsymbol{s}}^{\boldsymbol{dq}}}_{\text{Fundamental component}} + \underbrace{I_1\boldsymbol{I}_{\boldsymbol{s1}}^{\boldsymbol{\gamma}} + I_2\boldsymbol{I}_{\boldsymbol{s2}}^{\boldsymbol{\gamma}}}_{\text{Harmonic components}} \tag{6}$$

where $\boldsymbol{I}_{\boldsymbol{s1}}{}^{\gamma} = [\sin(-(n-1)\theta_e/n+\varphi_1)\ \cos(-(n-1)\theta_e/n+\varphi_1)]^T$ is the harmonics with the frequency of $(n-1)\omega_e/n$, and $\boldsymbol{I}_{\boldsymbol{s2}}{}^{\gamma} = [\sin(-(2n-1)\theta_e/n+\varphi_2)\ \cos(-(2n-1)\theta_e/n+\varphi_2)]^T$ is the harmonics with the frequency of $(2n-1)\omega_e/n$.

According to (2) and (6), the relationship of current vectors in *dq*-axis, $\alpha\beta$-axis, and $\alpha^{\gamma}\beta^{\gamma}$-axis frames is shown in Fig. 2. As can be seen, the first harmonic vector of *dq*-axis frame is stationary with respect to the $\alpha\beta$-axis frame with the amplitude of I_1, which is expressed as the current offset in the $\alpha\beta$-axis frame. The second harmonic rotates at the same frequency and the opposite direction as the fundamental current vector in the $\alpha\beta$-axis frame, resulting in the amplitude of the second harmonic coupled to that of the fundamental vector [15]. In the $\alpha^{\gamma}\beta^{\gamma}$-axis frame, the current vector can be expressed as the fundamental component with the frequency ω_e/n and the harmonics with the frequencies $(n-1)\omega_e/n$ and $(2n-1)\omega_e/n$. Hence, the fundamental and harmonic frequencies are decoupled in the $\alpha^{\gamma}\beta^{\gamma}$-axis system, and the fundamental component can be obtained by filtering out the harmonics.

The $\alpha^{\gamma}\beta^{\gamma}$-axis currents after filtering can be obtained through the single-frequency harmonic suppressor. Then, the *dq*-axis currents without harmonics can be acquired by the transformation matrix with angle θ_e/n as

$$\boldsymbol{i}_{\boldsymbol{s}}^{\boldsymbol{dq}} = \boldsymbol{T}_{\boldsymbol{sr}}(\theta_e/n)\cdot \boldsymbol{i}_{\boldsymbol{sf}}^{\boldsymbol{\gamma}} \tag{7}$$

where $\boldsymbol{i}_{\boldsymbol{sf}}^{\boldsymbol{\gamma}} = [i_{\alpha f}^{\gamma} i_{\beta f}^{\gamma}]^T$is $\alpha^{\gamma}\beta^{\gamma}$-axis currents after filtering, $\boldsymbol{T}_{\boldsymbol{rs}}(\theta_e/n)$ is the transformation matrix with θ_e/n shown as

$$\boldsymbol{T}_{\boldsymbol{sr}}(\theta_e/n) = \begin{bmatrix} \cos(\theta_e/n) & \sin(\theta_e/n) \\ -\sin(\theta_e/n) & \cos(\theta_e/n) \end{bmatrix}. \tag{8}$$

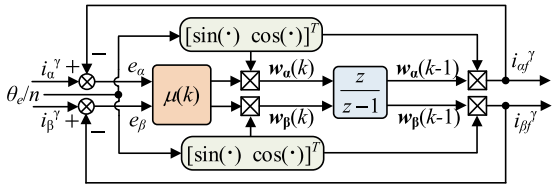

Fig. 3. Structure diagram of the single-frequency harmonic suppressor.

B. Single-Frequency Harmonic Suppressor

In the $\alpha^{\gamma}\beta^{\gamma}$-axis frame, $\boldsymbol{i}_{\boldsymbol{sf}}^{\boldsymbol{\gamma}}$ in (7) is obtained by the single-frequency harmonic suppressor, which is established according to the least mean square method. The $\alpha^{\gamma}\beta^{\gamma}$ -axis current vector is used as the input, and the filter weights of $\alpha^{\gamma}\beta^{\gamma}$-axis currents are adjusted by adaptive iteration to achieve the fast convergence of the current vector error thus obtaining the fundamental current vector. The structure diagram of the single-frequency harmonic suppressor is shown in Fig. 3.

According to the principle of the Wiener filter [16], the fundamental component of the current can be expressed by the product of the unit vector and the weight coefficient

$$\begin{aligned} \boldsymbol{i}_{\boldsymbol{sf}}^{\boldsymbol{\gamma}} &= \boldsymbol{w}\,(k)\,\boldsymbol{X}^T\,(k) \\ &= \left[\, w_{\alpha}(k)\ w_{\beta}(k) \,\right]\left[\, \sin\left(\theta_e/n\right)\ \cos\left(\theta_e/n\right) \,\right]^T \end{aligned} \tag{9}$$

where $\boldsymbol{w}(k) = [w_{\alpha}(k)\ \mathrm{w}_{\beta}(k)]$ is the weight coefficients of the fundamental vector, $\boldsymbol{X}^T(k) = [\sin(\theta_e/n)\ \cos(\theta_e/n)]^T$ is the projection vector of the unit fundamental current vector on the $\alpha^{\gamma}\beta^{\gamma}$-axis frame, the unit of which is A. The error sequence can be shown as

$$\boldsymbol{e}_{\boldsymbol{s}}(k) = \left[i_{\alpha}^{\gamma}(k) - i_{\alpha f}^{\gamma}(k) i_{\beta}^{\gamma}(k) - i_{\beta f}^{\gamma}(k) \right]^T \tag{10}$$

where $\boldsymbol{e}_{\boldsymbol{s}}(k) = [i_{\alpha}{}^{\gamma}(k) - i_{\alpha f}{}^{\gamma}(k)\ i_{\beta}{}^{\gamma}(k) - i_{\beta f}{}^{\gamma}(k)]$ is the error between $\alpha^{\gamma}\beta^{\gamma}$-axis currents before and after filtering.

$\boldsymbol{e}_{\boldsymbol{s}}(k)$ in (10) represents the whole harmonic components. When $\boldsymbol{e}_{\boldsymbol{s}}(k)$ takes the minimum value, it means that the harmonic components have been fully extracted and filtered. The mean square deviation $\xi = E[\boldsymbol{e}_{\boldsymbol{s}}{}^2(k)]$ is chosen as the cost function. Thus, when ξ reaches the minimum, the fundamental vector can be obtained effectively. Suppose ∇J be the gradient vector of each iteration. Taking the partial derivative of the cost function with respect to the weight coefficient, the expression of ∇J can be shown as

$$\nabla J = \frac{\partial E[\boldsymbol{e}_{\boldsymbol{s}}^2(k)]}{\partial \boldsymbol{w}(k)} = \frac{\partial \boldsymbol{e}_{\boldsymbol{s}}^2(k)}{\partial \boldsymbol{w}(k)} = -2\boldsymbol{e}_{\boldsymbol{s}}(k)X(k) \tag{11}$$

where $\mu(k)$ is the length of the convergence step, whose meaning is the convergence speed that minimizes ξ. The weight coefficient should be adjusted in the direction of minimum error. Hence, the iterative function of the weight coefficient is

$$w(k+1) = w(k) + 2\mu(k)\nabla J = w(k) + 2\mu(k)e_s(k)X(k). \tag{12}$$

It can be illustrated that ∇J is adjusted by the error vector, thus the adaptive iterative adjustment of the weight can be realized. Through (9) and (10), the amplitude decay ratio of the filter

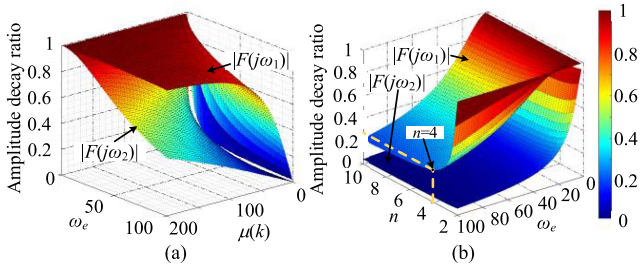

Fig. 4. Harmonic amplitude decay ratio surface as parameter changes. (a) Change of speed and convergence step. (b) Change of speed and n.

$|F(j\omega)|$ is obtained as

$$|F(j\omega)| = \mu(k)\omega \Big/ \sqrt{\mu^2(k)\omega^2 + \left(\omega_e^2/n^2 - \omega^2\right)^2}. \quad (13)$$

The frequencies of the current harmonics in the $\alpha^\gamma\beta^\gamma$-axis frame are $(n-1)\omega_e/n$ and $(2n-1)\omega_e/n$. Substituting the harmonic frequencies into (12) and calculating the amplitude decay ratio. The change of the amplitude decay ratio of the harmonics when the parameters changes is shown in Fig. 4, where $|F(j\omega_1)|$ is the amplitude decay ratio with the frequency of $(n-1)\omega_e/n$, and $|F(j\omega_2)|$ is the amplitude decay ratio with the frequency $(2n-1)\omega_e/n$.

Fig. 4(a) shows the change surface of the amplitude decay ratio as ω_e and $\mu(k)$ change. When $\mu(k)$ is constant and ω_e increases, the amplitude decay ratio gradually decreases. When ω_e is constant and $\mu(k)$ increases, the filtering effect becomes worse, indicating that smaller value of the convergence step is beneficial to the filtering. Fig. 4(b) shows the amplitude decay ratio when n and ω_e change where $\mu(k) = 10$. The change effect on the filtering effect is not significant when $n \geq 4$. Thus, the suggested value of n is 4.

However, it can be noticed from Fig. 4 that the filtering effect diminishes as the speed decreases with the fixed value of $\mu(k)$. In order to obtain the ideal filtering effect at different speeds, the variable step size of the convergence is used in the suppressor. As shown in Fig. 4, the amplitude decay ratio of $(n-1)\omega_e/n$th harmonic is larger than that of $(2n-1)\omega_e/n$ harmonic under the same conditions. Therefore, the amplitude decay ratio of $(2n-1)\omega_e/n$th harmonic is smaller than that of $(n-1)\omega_e/n$th harmonic as long as the parameters are designed for $(n-1)\omega_e/n$th harmonic. The amplitude decay ratio of $(n-1)\omega_e/n$th harmonic is expressed as

$$|F(j\omega_1)| = \mu(k)(n-1) \Big/ \sqrt{\mu^2(k)(n-1)^2 + (n-2)^2\omega_e^2}. \quad (14)$$

Therefore, the convergence step can be adjusted by setting the harmonic decay ratio, and the value of the convergence step can be obtained as

$$\mu(k) = (n-2)\omega_e \Big/ \left((n-1)\sqrt{1/|F(j\omega_1)|^2 - 1}\right). \quad (15)$$

As can be seen from (15), $\mu(k)$ changes down as $F(j\omega_1)$ decreases, which means that smaller harmonic content will achieve slower convergence speed. Hence, it is necessary to weigh the convergence speed and the convergence effect.

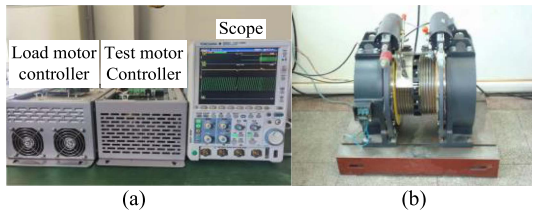

Fig. 5. Experimental platform. (a) Controllers. (b) PMSM.

TABLE I
PMSM PARAMETERS

Parameter	Value	Parameter	Value
Rated Power	11.7 kW	Rated Torque	670 N·m
Rated Speed	167 r/min	Rated Current	23 A
Rated Frequency	33.4 Hz	Resistance	0.23 Ω
Rated Voltage	380 V	Number of Pole Pairs	12

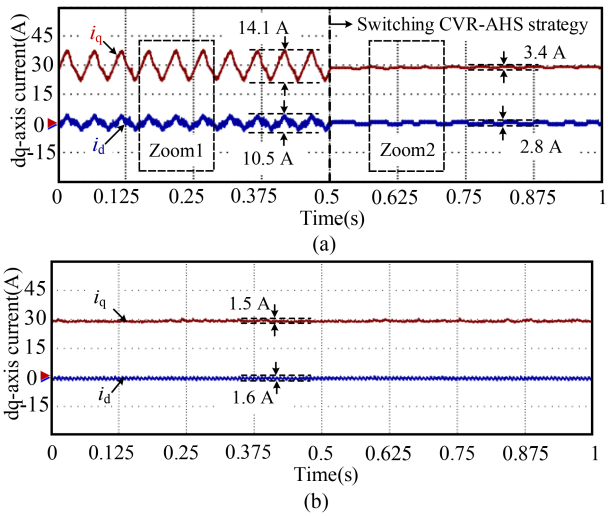

Fig. 6. Experimental waveforms of dq-axis currents. (a) Without and with the proposed CVR-AHS strategy. (b) Without the CMEs.

III. Experimental Results

The proposed CVR-AHS strategy is verified on the PMSM drive platform in Fig. 5. The parameters of PMSM are shown in Table I. The whole control algorithm is executed in the ARM chip STM32F103VB. The switching frequency of the inverter is 6 kHz, and the periods of the current and speed loops are 166.7 μs and 1 ms, respectively.

Fig. 6(a) shows the experimental waveforms of dq-axis currents without and with the CVR-AHS strategy, and Fig. 6(b) shows the dq-axis currents without the CMEs to be the reference of the filtering effect. In this case, $I_{\mathrm{AM}} = 0.8$ p.u., $C_A = 0.2$ p.u., $n = 4$, and $F(j\omega_1) = 0.25$. It can be observed that the q-axis current fluctuation decreases from 14.1 to 3.4 A, showing the harmonic suppression rate of 75.9% with the proposed method. The d-axis

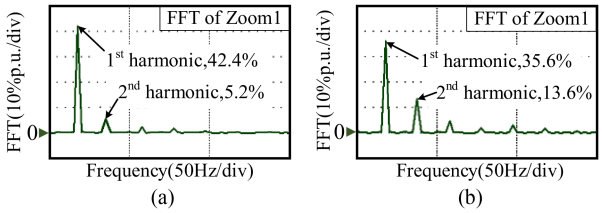

Fig. 7. FFT analysis without CVR-AHS. (a) q-axis current. (b) d-axis current.

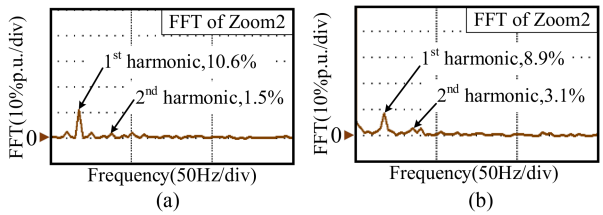

Fig. 8. FFT analysis with CVR-AHS. (a) q-axis current. (b) d-axis current.

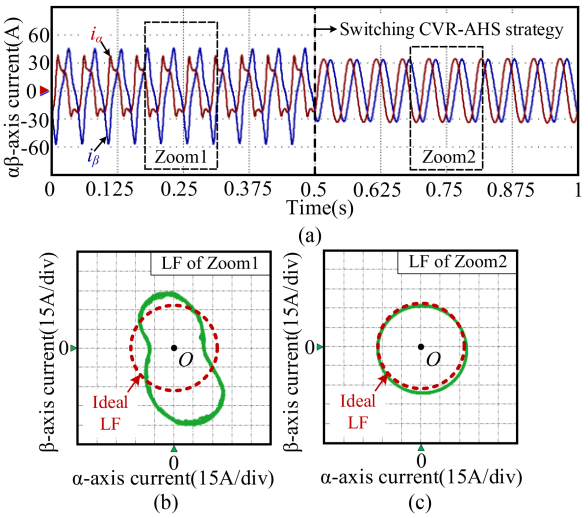

Fig. 9. Experimental waveforms of $\alpha\beta$-axis currents. (a) Whole waveforms. (b) LF without CVR-AHS. (c) LF with CVR-AHS.

current fluctuation decreases from 10.5 to 2.8 A, showing the harmonic suppression rate of 73.3% with the proposed method.

Figs. 7 and 8 show the FFT analysis of dq-axis currents, which show that the dq-axis currents are dominated by the first and second current harmonics of the operating frequency. After the proposed method, the first harmonic component of the q-axis current is reduced from 42.4% to 10.6%, and the second harmonic component is reduced from 5.2% to 1.5%. The first harmonic component of the d-axis current is reduced from 35.6% to 8.9%, and the second harmonic component is reduced from 13.6% to 3.1%, which suppresses the current harmonics effectively.

Fig. 9 shows the experimental waveforms of the $\alpha\beta$-axis currents without and with the CVR-AHS strategy, where the proposed strategy is switched at 0.5 s to verified the steady-state effectiveness. The sinusoidality of $\alpha\beta$-axis currents can be effectively improved with the proposed method. Fig. 9(b) and (c)

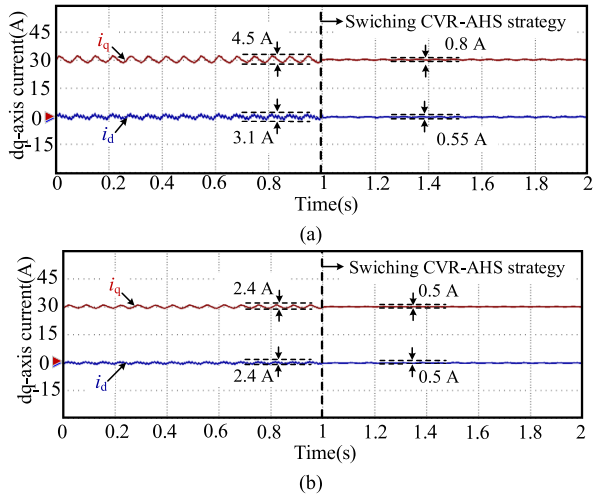

Fig. 10. Experimental waveforms of dq-axis currents under different gain and offset errors. (a) $I_{\mathrm{AM}} = 0.9$ p.u., $C_A = 0.1$ p.u. (b) $I_{\mathrm{AM}} = 0.95$ p.u., $C_A = 0.05$ p.u.

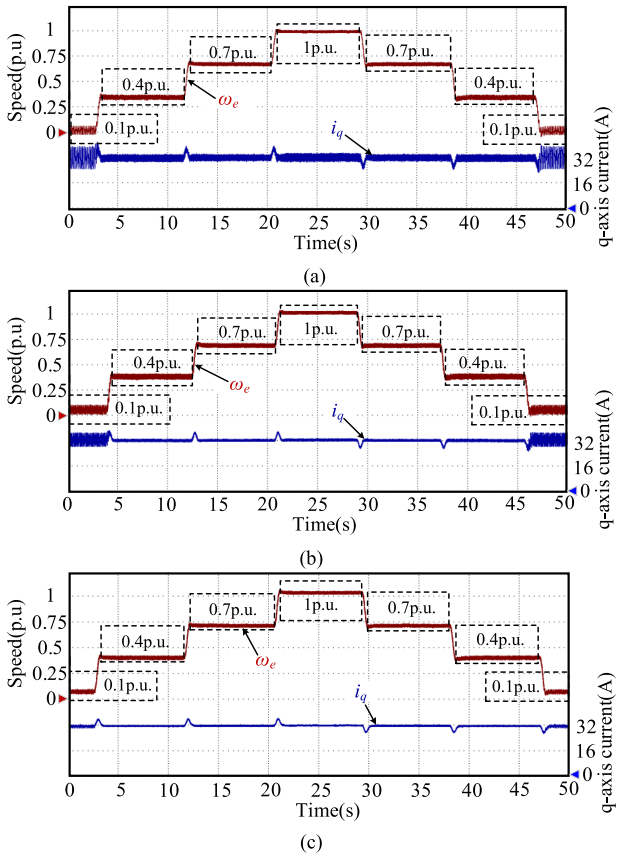

Fig. 11. Experimental results at step speed reference. (a) Without harmonic suppressor. (b) With classic LMS filter. (c) With proposed strategy.

shows the Lissajous figure (LF) without and with the CVR-AHS strategy, where the red line is the LF of $\alpha\beta$-axis currents without harmonics meaning the ideal current vector circle. It can be seen that the LF of $\alpha\beta$-axis currents with the proposed method is close to the ideal current vector circle, which proves that the harmonics in the current are effectively filtered out.

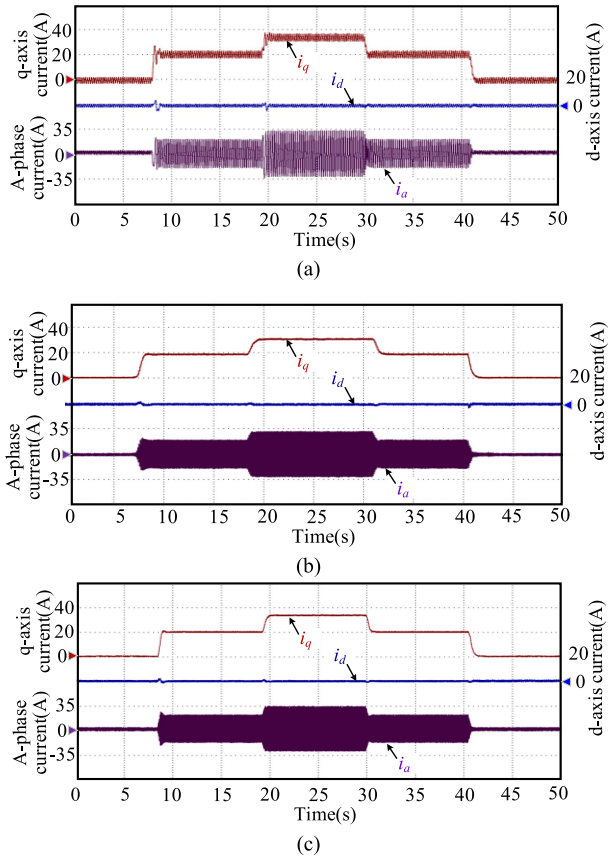

Fig. 12. Experimental results at step load torque reference. (a) Without harmonic suppressor. (b) With classic LMS filter. (c) With proposed strategy.

In order to be more consistent with the actual measurement error, the experimental results of the different CMEs are shown in Fig. 10. Fig. 10(a) is the experimental result at $I_{\mathrm{AM}} = 0.9$ p.u., $C_A = 0.1$ p.u., and Fig. 10(b) is the experimental result at $I_{\mathrm{AM}} = 0.95$ p.u., $C_A = 0.05$ p.u. In this case, $n = 4$, and $F(j\omega_1) = 0.25$. It can be seen that using the proposed strategy can suppress the dq-axis current harmonic effectively at different CMEs.

Fig. 11 shows the experimental results at the step speed, where the speed reference is 0.1 p.u.-0.4 p.u.-0.7 p.u.-1 p.u. of the rated speed, and the load is the rated torque. In this case, I_{AM}=0.9 p.u., C_A=0.2 p.u., n=4, and $F(j\omega_1)$=0.25. Seeing the comparison of Fig. 11(a) and (c), q-axis current fluctuation is effectively suppressed after the proposed method. The filtering effect can be automatically adjusted with the change of speed to ensure that the dq-axis currents fluctuation can be eliminated adaptively.

The classic LMS filter is used to suppress the harmonics in the dq-axis current. However, the complex structure and parameters make the classic LMS filter difficult to implement in practical application. Fig. 11(b) shows the experimental results of the classic LMS filter. Since the classic LMS filtering algorithm adopts the fixed step, the filtering effect is different for the changing speed. When the motor runs at low speed, the filtering effect is worse. As the speed increases, the harmonics can be effectively filtered. After using the proposed algorithm, the dq-axis current harmonics at different speeds can be suppressed.

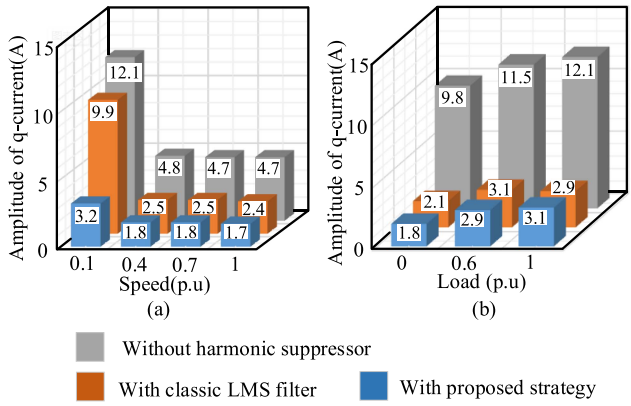

Fig. 13. Experimental statistics of filtering effect under different speeds and loads conditions.

Fig. 12 shows the experimental results at the step load torque, where the load torque is 0%−60%−100%−60%−0% of the rated load torque, and the speed reference is 0.5 p.u. In this case, $I_{\mathrm{AM}} = 0.8$ p.u., $C_A = 0.2$ p.u., $n = 4$, and $F(j\omega_1) = 0.25$. As can be seen from Fig. 12, both the classic LMS filter and the proposed strategy can achieve better filtering effect under different torque due to the constant speed reference.

In the experiment, the program execution time of the classic LMS filter and the proposed strategy is measured. The execution time of the classic LMS method is 23.27 μs, and the execution time of the proposed method is 5.24 μs showing that the structure of the proposed algorithm is simpler and easier to implement.

Fig. 13 shows the experimental statistics of the filtering effect under different speeds and loads conditions. It can be seen that the classic LMS algorithm can achieve a certain harmonic suppression effect when the speed changes. However, the filtering effect is different as the changing speed, where the filtering effect weakens with the decrease of the speed due to the convergence of fixed step. Since the convergence step can be adjusted adaptively with the speed, the proposed method can achieve ideal filtering effect under different speeds. Under different load torque, both the classic LMS filter and the proposed algorithm can obtain effective filtering effect.

IV. Conclusion

This letter has proposed an adaptive-frequency harmonic suppression strategy based on the current vector reconstruction for the CMEs of PMSM drives. The proposed method has taken the current vector reconstruction coordinate system as the framework, which can decouple the fundamental and harmonic components of the current vector in frequency. Within the reconstruction coordinate frame, a single-frequency harmonic suppressor has been adopted, which can filter the harmonics according to the change of the speed. Meanwhile, the convergence step can be adjusted adaptively with the speed so that the ideal filtering effect can be obtained at different speeds. The proposed method does not require the motor parameters and the complex computational procedures. Experiments on the 11.7-kW PMSM drive platform demonstrate the effectiveness of the proposed method.

REFERENCES

[1] Y. Bai, G. Wang, G. Zhang, N. Zhao, and D. Xu, "Position and speed detection method based on cross-decoupling network filtering for gearless traction motor drives at low-speed operation," *IEEE Trans. Power Electron.*, vol. 36, no. 10, pp. 11862–11874, Oct. 2021.

[2] K. Zhang, M. Fan, Y. Yang, Z. Zhu, C. Garcia, and J. Rodriguez, "An improved adaptive selected harmonic elimination algorithm for current measurement error correction of PMSMs," *IEEE Trans. Power Electron.*, vol. 36, no. 11, pp. 13128–13138, Nov. 2021.

[3] Y. Wang, Y. Gao, C. Zhao, and X. Li, "Iterative learning based torque ripple suppression of flux-modulation double-stator machine," *IEEE Trans. Ind. Electron.*, vol. 69, no. 7, pp. 6645–6656, Jul. 2022.

[4] B. Han, S. -W. Jo, M. Kim, N. A. Dung, and J. -S. Lai, "Improved odd-harmonic repetitive control scheme for Ćuk-derived inverter," *IEEE Trans. Power Electron.*, vol. 37, no. 2, pp. 1496–1508, Feb. 2022.

[5] N. Zhao, G. Wang, D. Xu, L. Zhu, G. Zhang, and J. Huo, "Inverter power control based on dc-link voltage regulation for IPMSM drives without electrolytic capacitors," *IEEE Trans. Power Electron.*, vol. 33, no. 1, pp. 558–571, Jan. 2018.

[6] S. A. Q. Mohammed, A. T. Nguyen, H. H. Choi, and J. -W. Jung, "Improved iterative learning control strategy for surface-mounted permanent magnet synchronous motor drives," *IEEE Trans. Ind. Electron.*, vol. 67, no. 12, pp. 10134–10144, Dec. 2020.

[7] Y. Ge, L. Yang, and X. Ma, "A harmonic compensation method for SPMSM sensorless control based on the orthogonal master-slave adaptive notch filter," *IEEE Trans. Power Electron.*, vol. 36, no. 10, pp. 11701–11711, Oct. 2021.

[8] H. Cheng, S. Sun, X. Zhou, D. Shao, S. Mi, and Y. Hu, "Sensorless DPCC of PMLSM using SOGI-PLL-based high-order SMO with cogging force feedforward compensation," *IEEE Trans. Transp. Electrific.*, vol. 8, no. 1, pp. 1094–1104, Mar. 2022.

[9] L. Wang, Z. Q. Zhu, H. Bin, and L. M. Gong, "Current harmonics suppression strategy for PMSM with nonsinusoidal back-EMF based on adaptive linear neuron method," *IEEE Trans. Ind. Electron.*, vol. 67, no. 11, pp. 9164–9173, Nov. 2020.

[10] A. T. Woldegiorgis, X. Ge, H. Wang, and M. Hassan, "A new frequency adaptive second-order disturbance observer for sensorless vector control of interior permanent magnet synchronous motor," *IEEE Trans. Ind. Electron.*, vol. 68, no. 12, pp. 11847–11857, Dec. 2021.

[11] G. Zhang, G. Wang, D. Xu, and N. Zhao, "ADALINE-network-based PLL for position sensorless interior permanent magnet synchronous motor drives," *IEEE Trans. Power Electron.*, vol. 31, no. 2, pp. 1450–1460, Feb. 2016.

[12] D. Xiao, S. Nalakath, Y. Sun, J. Wiseman, and A. Emadi, "Complex-coefficient adaptive disturbance observer for position estimation of IPMSMs with robustness to DC errors," *IEEE Trans. Ind. Electron.*, vol. 67, no. 7, pp. 5924–5935, Jul. 2020.

[13] D. Xiao et al., "Computation-efficient position estimation algorithm for permanent magnet synchronous motor drives under distorted conditions," *IEEE Trans. Emerg. Sel. Topics Power Electron.*, vol. 9, no. 3, pp. 2759–2773, Jun. 2021.

[14] Y. Ge, L. Yang, and X. Ma, "A harmonic compensation method for SPMSM sensorless control based on the orthogonal master-slave adaptive notch filter," *IEEE Trans. Power Electron.*, vol. 36, no. 10, pp. 11701–11711, Oct. 2021.

[15] Q. Zhang et al., "An adaptive proportional-integral-resonant controller for speed ripple suppression of PMSM drive due to current measurement error," *Int. J. Elect. Power Energy Syst.*, vol. 129, 2021, Art. no. 106866.

[16] M. Zhang, A. Zhang, and J. Li, "Fast and accurate rank selection methods for multistage wiener filter," *IEEE Trans. Signal Process.*, vol. 64, no. 4, pp. 973–984, Feb. 2016.